

Article

Study of the Performance Enhancement of Sc-Doped AlN Super High Frequency Cross-Sectional Lamé Mode Resonators

Meruyert Assylbekova ^{*}, Michele Pirro , Xuanyi Zhao , Giuseppe Michetti , Pietro Simeoni and Matteo Rinaldi

SMART Center, Northeastern University, Boston, MA 02115, USA

* Correspondence: assylbekova.m@northeastern.edu

Abstract: The increasing use of mobile broadband requires new acoustic filtering technologies that can operate efficiently at frequencies above 6 GHz. Previous research has shown that AlN Super High Frequency (SHF) Cross-Sectional Lamé Mode resonators (CLMRs) can address this challenge, but their performance is limited by the piezoelectric strength of AlN. In this work, we explore the use of substitutional doping of Al in AlN with Sc to enhance the k_t^2 values of SHF CLMRs. Our results showed that the measured $k_t^2 \cdot Q_m$ product of Al₇₂Sc₂₈N CLMRs was four times greater than that of AlN CLMRs operating at the same frequency. Additionally, the measured fractional bandwidth (FWB) of Al₇₂Sc₂₈N 2nd order ladder filters was 4.13%, a fourfold improvement over AlN filters with the same design. We also discuss other aspects of the technology, such as power handling, losses, and spurious mode suppression, and identify potential areas for future research.

Keywords: AlScN; MEMS resonators; Contour Lamé Mode resonators; beyond 6 GHz; piezoelectric



Citation: Assylbekova, M.; Pirro, M.; Zhao, X.; Michetti, G.; Simeoni, P.; Rinaldi, M. Study of the Performance Enhancement of Sc-Doped AlN Super High Frequency Cross-Sectional Lamé Mode Resonators. *Micromachines* **2023**, *14*, 515. <https://doi.org/10.3390/mi14030515>

Academic Editor: Fabio Di Pietrantonio

Received: 22 January 2023

Revised: 19 February 2023

Accepted: 21 February 2023

Published: 23 February 2023



Copyright: © 2023 by the authors. Licensee MDPI, Basel, Switzerland. This article is an open access article distributed under the terms and conditions of the Creative Commons Attribution (CC BY) license (<https://creativecommons.org/licenses/by/4.0/>).

1. Introduction

With almost all of the sub 6 GHz spectrum now being allocated, current bandwidth shortage has motivated the exploration of untapped frequencies beyond 6 GHz for future broadband wireless communication. A shift to higher frequency spectra is expected to deliver significant performance improvement in network capacity, data rates, and latency. Among a variety of novel 5G applications, the implementation of 5G mobile broadband imposes especially demanding specifications on Radio Frequency (RF) front end architectures. It is expected that 5G smartphones will carry over the legacy sub 6 GHz bands, which translates into an increased number of filters.

The majority of acoustic filters in the traditional RF front end architecture are formed by either surface acoustic wave (SAW) resonators or film bulk acoustic wave resonators (FBARs). These acoustic filtering technologies replaced their electromagnetic (EM) predecessors due to their small form factor, low cost and high performance. SAW filters have been utilized widely because of the simple process flow and better power handling. However, SAW filters face performance issues above 2 GHz, due to acoustic wave propagation losses, that do not affect FBAR filters until higher frequencies [1]. FBARs, on the other hand, relying on a thickness-extensional mode, provide only a single frequency per AlN deposition. Implementation of multi-frequency FBARs requires additional fabrication steps, such as mass-loading or trimming, which increase fabrication costs. Furthermore, scaling of FBARs to operate above 6 GHz incurs performance degradation, due to the reduced crystal quality in thin piezoelectric films [2]. At this point, neither technology appears to be a viable option for the implementation of future RF front ends operating above 6 GHz.

The development of acoustic filters by exploiting advancements in thin film processing and vibrational modes at higher frequencies is a promising solution to the realization of high-quality beyond-6 GHz miniature acoustic filters. For example, Super High Frequency (SHF) AlN Contour-Mode resonators (CMRs) were shown to operate in the 5–10 GHz

range [3] with a loaded quality factor (Q) equal to 740. CMRs are attractive for operation at high frequencies given their demonstrated moderate Q values and lithographic tunability. However, their electromechanical coupling coefficient, k_t^2 , values are limited, due to the weak piezoelectric coupling of the contour-extensional mode in AlN. Resonance at 33 GHz was demonstrated in AlN FBAR operating in a second overtone with measured loaded Q equal to 110 and 1.7% k_t^2 [4]. While the overtone FBAR was fabricated using thicker piezoelectric film compared to the first mode scaled to the same frequency, its k_t^2 significantly reduced as the mode number increased. AlN Cross-Sectional Lamé Mode Resonators (CLMRs) [5] were demonstrated to operate at 11 GHz with 1.3% and loaded Q equal to 615. Credited to the combined use of d_{33} and d_{31} piezoelectric coefficients of AlN [6], CLMRs offer both strong electromechanical coupling and wafer-level frequency diversity. Although AlN CLMRs can achieve k_t^2 as highly as AlN FBARs along with lithographic frequency tuning (Δf), their maximum k_t^2 is still insufficient to accommodate ultra-wide bandwidths at high frequencies. Strong k_t^2 is especially useful for high frequencies where Q values are generally lower [7] and extra headroom in k_t^2 can be used to compensate for lower Q .

In the last decade, the MEMS community benefited from the discovery of $\sim 4\times$ enhancement of electromechanical coupling through substitutional doping of Al in AlN with Sc [8]. Specifically, it has demonstrated high k_t^2 at resonance up to 6 GHz [9,10]. However, for resonators with frequency (f_{res}) above-6 GHz, k_t^2 values have still been below 5%, with degraded Q -values [11,12]. In this work, we show that by doping AlN with moderate Sc concentration (28%) and maintaining a relatively high Q factor, almost a $4\times$ improvement in Figure of Merit ($FoM = k_t^2 \cdot Q$) was achieved over AlN CLMR. To pursue better designs, energy loss mechanisms relevant at frequencies beyond 6 GHz, along with power handling and spurious mode suppression, are studied. While energy loss mechanism becomes nontrivial at the SHF range, an improved resonator geometry is identified for spurious mode suppression and better power handling. The total demonstrated lithographic Δf capability was over 5 GHz. Lastly, $Al_{72}Sc_{28}N$ second order ladder type filter was implemented with a fractional bandwidth (FBW) exceeding that of AlN fourfold, thus opening up new possibilities for wireless communication beyond 6 GHz.

2. Super High Frequency AlScN CLMRs

2.1. k_t^2 and Frequency Tuning Dependence on the Design

Cross-Sectional Lamé Mode resonators (CLMRs) introduced in [6] operate based on the piezoelectric transduction of a cross-sectional Lamé mode in an AlN plate characterized by longitudinal vibrations along both the thickness and the lateral directions. CLMRs can be excited through either thickness field excitation (TFE) requiring top and bottom interdigital metal electrodes (IDTs) or through lateral field excitation (LFE) with only top IDTs. Although a TFE scheme grants higher k_t^2 values, there are challenges associated with depositing good quality piezoelectric films on bottom metal electrodes [13]. An LFE scheme, on the other hand, allows for a simplified fabrication process, which reduces production costs. Figure 1a shows the 3D geometry of the LFE CLMR considered in this work. The maximum k_t^2 value is achieved upon excitation of the so-called non-degenerate Lamé mode. This non-degeneracy condition is met when the pitch, W , is approximately equal to the thickness of the piezoelectric layer, T . Pitch of the IDT defines the resonant frequency similarly to Lamb wave resonators (LWRs) and is equal to a half of the longitudinal wavelength (λ). However, while LWRs are based on the excitation of the lowest-order symmetric (S_0) mode solely in the lateral direction (along the x -axis), the CLMR mode is excited when S_0 mode resonance frequency matches that of S_0 mode propagating in the vertical direction (along the z -axis).

To excite the S_0 mode in both directions, λ_x / T_{AlN} has to satisfy the following equality as was shown in [6].

$$\frac{\lambda_x}{T_{AlN}} = 2\sqrt{\frac{C_{11} - C_{55}}{C_{33} - C_{55}}} \quad (1)$$

When this bidirectional resonance takes place, there is an observed peak-to-peak displacement along lateral (μ_x) and vertical (μ_z) directions that are approximately the same. This mutual displacement takes advantage of both, d_{31} and d_{33} , piezoelectric coefficients resulting in higher k_t^2 compared to CMRs that rely solely on d_{31} coefficient [6]. Figure 1b demonstrates the simulated k_t^2 over a range of pitch values, while AlN and Al top electrode thickness was fixed at 383 nm and 40 nm, respectively. Dimensions of the pitch values and AlN thickness were chosen so to achieve resonance at around 11 GHz. The same figure also shows the vibrational modes corresponding to each pitch value. Maximum k_t^2 equal to 2.38 % was achieved when $W = 415$ nm. The same figure shows an interesting change in the mode shape as the pitch value changed. When $W > 415$ nm, the mode shape gradually resembled that of the contour mode. This happened because the lateral electric field became stronger compared to the electric field in the vertical direction. Conversely, when $W < 415$ nm, the lateral field strength reduced and the mode shape gradually started to resemble the thickness mode.

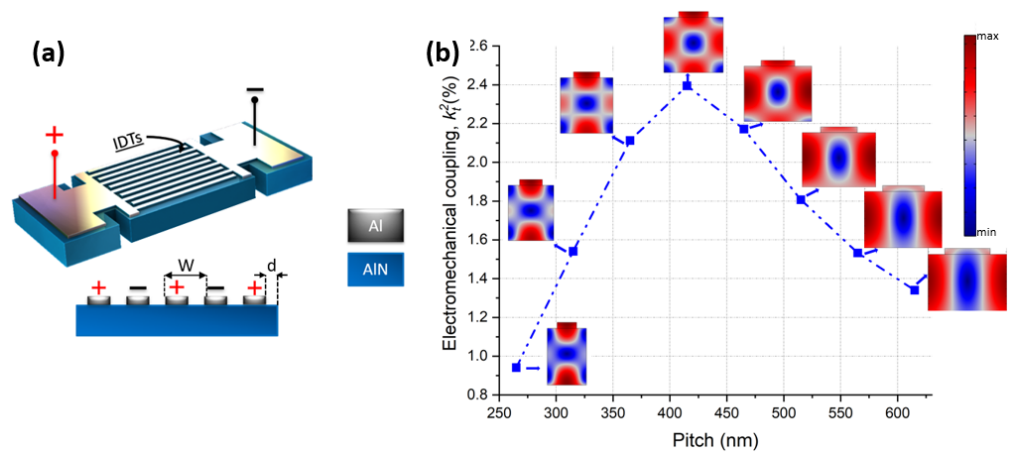


Figure 1. (a) CLMR geometry in 3D. (b) Simulated k_t^2 over a range of pitch values with corresponding mode shapes.

The aforementioned observation could be supported through a visual comparison of displacement magnitudes in a single unit cell with fixed AlN thickness and varying pitch length. Figure 2a plots μ_x for each pitch value. As expected, the magnitude of μ_x increased with increased pitch length. Conversely, Figure 2b shows that displacement in the thickness direction, μ_z , became larger as the pitch length became smaller. Slight deviation from the optimal λ_x / T_{AlN} , however, can be used for lithographic frequency tuning.

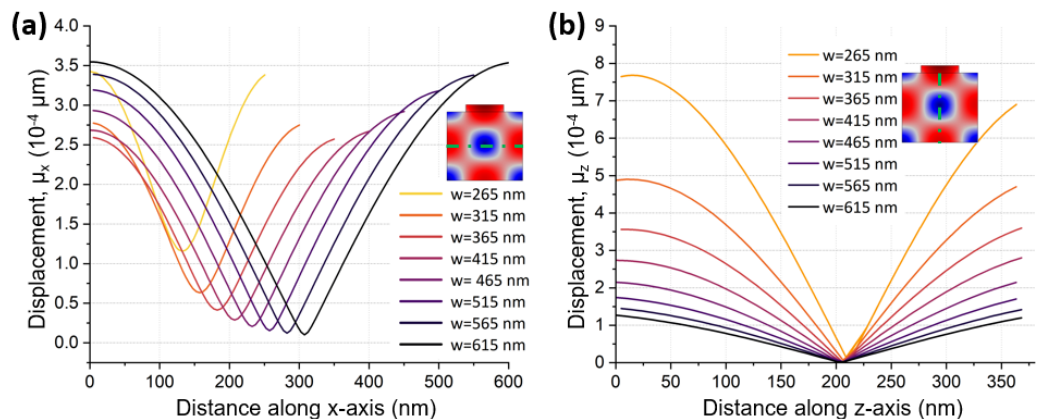


Figure 2. (a) Simulated displacement (μ_x) along the dotted cut line on the x-axis. (b) Simulated displacement (μ_z) along the dotted cut line on the z-axis. Data is simulated in Comsol®2D (ver. 5.6, Boston, MA, USA) for a fixed AlN and top metal thicknesses (383 nm and 40 nm, respectively).

Similarly, there was optimal λ_x / T_{AlScN} when doping AlN with Sc. Due to increased piezoelectric strength with the addition of Sc, optimal λ_x / T_{AlN} could give significantly higher k_t^2 values in comparison to AlN. Akiyama et al. demonstrated that when AlN was doped with Sc, d_{33} piezoelectric coefficient of AlScN was 500% higher than d_{33} of AlN for Sc concentrations between 40% and 45% [8]. The CLMRs reviewed in this study were based on AlScN with 28% Sc concentration. The predicted maximum k_t^2 for 28% Sc concentration was nearly three-fold that of AlN, as shown in Figure 3a, where k_t^2 was simulated over a range of thickness over wavelength (h/λ_x) ratios for both AlN and $Al_{72}Sc_{28}N$ CLMRs. Specifically, the maximum k_t^2 of $Al_{72}Sc_{28}N$ CLMRs was 7.1%, in comparison to 2.38% for the AlN CLMRs. This work targeted resonance frequency around 11 GHz with the expected admittance response shown in Figure 3b. Since Young's modulus decreases with increased Sc content, the resonance frequency of AlScN devices is lower than that of AlN resonators for the same pitch dimensions.

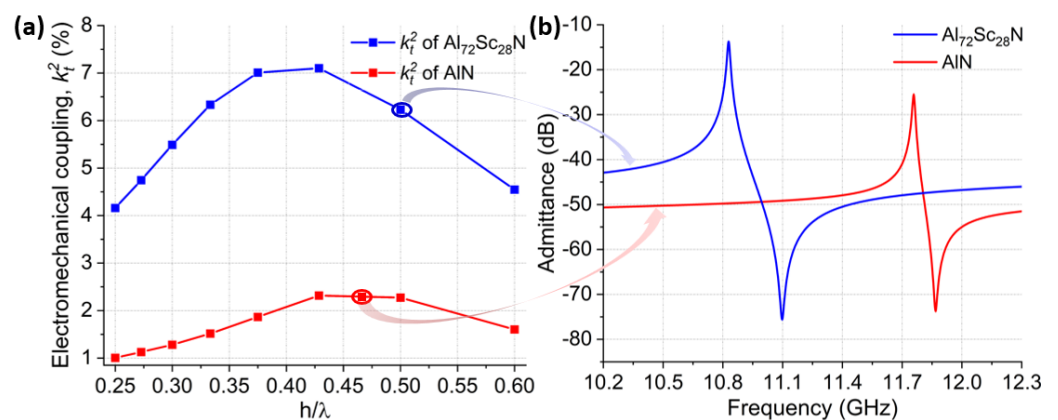


Figure 3. (a) Simulated k_t^2 of AlN (red) and AlScN (blue) over a range of h/λ_x values. (b) admittance response of AlN and $Al_{72}Sc_{28}N$ CLMRs operating around 11 GHz with the respective arrows indicating expected k_t^2 values.

While it is possible to accurately target a specific frequency and FoM, spurious modes appearing near the resonance are often challenging to predict and, ultimately, degrade filter performance. Here, we draw attention to a specific CLMR design parameter, namely, the “overhang”, which is a dimension measured from the edge of the outermost electrode finger to the edge of the piezoelectric plate and is labeled as d in Figure 1a. It has been shown that the dimension d , if improperly set, can contribute to the generation of unwanted spurious modes [14]. The main mode of the CLMR corresponds to a bidirectional coupling of acoustic waves traveling in lateral and vertical directions, which are in-phase. Dimension d needs to be such that it guarantees maximum displacement at the reflection boundary and in-phase displacement in both directions. It is demonstrated that in-phase condition was disrupted for a specific set of d values, resulting in the main mode being split into two smaller ones, as the trapped energy needed to be redistributed. The in-phase condition was luckily restored for a different set of d values.

SHF CLMRs are in the early stage of their development and need to be studied more comprehensively. Hence, along with the demonstration of good performance at super high frequency this work also encompasses a number of studies, such as a nonlinearity study and a study on relevant energy losses. Performance metrics, such as power handling and temperature coefficient of frequency, are crucial for successful commercialization and are also assessed in this work. Additionally, frequency tunability and impedance scaling are reviewed, along with a demonstration of filter responses of both SHF AlN and AlScN ladder filters.

2.2. Quality Factor

Large Q factor is indicative of low dissipation in MEMS resonators and is defined as the ratio of the stored energy over the dissipated energy per harmonic cycle [15].

$$Q = 2\pi \frac{E_{\text{stored}}}{E_{\text{dissipated}}} \quad (2)$$

Increasing the Q factor of MEMS resonators is essential to achieve a low insertion loss in filters [16] and low phase noise in oscillators [17]. The damping coefficient, γ , is a measure of the linear dissipation in a mechanical structure and can be expressed as

$$\gamma = \frac{\sqrt{km}}{Q} \quad (3)$$

Equation (3) implies that a higher frequency resonator made of a soft material exhibits a smaller Q factor compared to its larger and stiffer counterpart. For fixed m and k coefficients, the Q factor can be increased by engineering the device geometry to reduce the dominant dissipative mechanisms. From Equation (2) it is apparent that, if no external energy is supplied or removed from the system, the Q factor is inversely proportional to the losses within the resonant structure. Several losses can affect the magnitude of the Q factor in a MEMS resonator and can be summarized as

$$\frac{1}{Q} = \frac{1}{Q_{el}} + \frac{1}{Q_{gas}} + \frac{1}{Q_{anchor}} + \frac{1}{Q_{TED}} + \frac{1}{Q_{p-p}} \quad (4)$$

The losses dominating in AlScN CLMRs operating in the SHF range could be due to a single dominant dissipative mechanism or due to a combination of a few of them.

Electrical losses ($1/Q_{el}$) are straightforward in definition and imply dissipation of electrical energy into heat in the metal electrodes. In general, thicker and lower resistance metals help to minimize these losses. Proper design of the electrodes can also aid in the reduction of such losses. In particular, the resistance of a metal routing (R_s) in a fully anchored LFE CLMR is simply estimated as $R = \rho L/Wt_m$, where ρ is the metal density, L and W is length and width, and t_m is the metal thickness. The resistance of metal IDTs can be represented as a parallel combination of resistances of each metal finger with the anchor as the connecting node. The total resistance of the metal IDTs can be expressed as

$$R_{IDT} = \frac{L_e \rho}{W_e t_m N} \quad (5)$$

where L_e , W_e and N are the length, pitch and number of IDT fingers, respectively. Due to the large aspect ratio (L_e/W_e) of the IDTs, R_{IDT} is expected to be the dominant part in the R_s estimation.

Viscous losses ($1/Q_{gas}$) are due to the transfer of some of the resonator's kinetic energy to the surroundings when the resonator's surface interacts with the ambient gas molecules. This type of loss is significant for low frequency relatively large resonant structures with large separation between the vibrating body and the substrate [18]. As the surface to volume ratio of the resonant device scales down, this type of loss becomes less dominant [19].

Anchor losses ($1/Q_{anchor}$) are caused by the leak of the acoustic energy through the anchors that attach the resonator to the substrate. Anchor losses have been shown to be significant for low frequency resonators [20,21], while for higher frequency resonators, when the acoustic wavelength becomes much smaller than the resonator size (>1 GHz), they become insignificant [21].

Thermoelastic damping ($1/Q_{TED}$) is a type of loss that happens through an irreversible heat flow from the local temperature gradient generated because of the induced volume change when the elastic solid vibrates. For example, compression of a solid generates increase in the temperature, while expansion results in the decrease of the local temperature. Conveniently, in nondegenerate Lamé modes, while there is an expansion in one direction

of motion, there is an equal contraction in the orthogonal direction. This leads to an interesting feature of the Lamé mode in having practically zero TED because of the zero net volume change [22]. The same might not hold true for the degenerate Lamé mode, which has an unequal displacement in orthogonal directions. TED, however, accounts for only 4% of the losses in semiconductor and dielectric devices vibrating in the extensional mode, while in metals about 50% of the losses was found to be due to the TED [23]. Segovia-Fernandez et al. [24] demonstrated TED dependence on thermal characteristics and the geometry of the metal electrodes (metal coverage) of AlN CMRs and its reduction at lower operating temperatures.

Phonon – phonon interaction-induced loss ($1/Q_{p-p}$) is another thermo-mechanical loss that has reciprocal dependence on the temperature, as in the case of TED. The two, however, differ in the way the equilibrium state of phonons is attained after being subjected to strain. In the TED case, equilibrium is achieved through the diffusive transport of heat, as opposed to the ballistic transport of phonons between hot and cold regions for loss due to phonon–phonon interactions [25]. Thus, $1/Q_{p-p}$ loss is considered local in its nature and is independent of the device geometry [26]. Phonon–phonon interaction is, in turn, divided into two regimes, based on the magnitude of the acoustic wavelength (λ) relative to the mean free path of phonons (τ). In the so-called Akheiser regime, when λ is significantly larger than the τ , it is assumed that the acoustic waves interact with a group of phonons and change their frequencies locally. In this regime, $f \cdot Q$ product, which is another important figure of merit in MEMS resonators, is constant for longitudinal acoustic waves [25]. When λ becomes smaller than τ , elastic phonons (acoustic quanta) start to interact with individual thermal phonons. This regime was named the Landau–Rumer regime and is characterized by the linear dependence of $f \cdot Q$ product on the operating frequency [27]. The transition between the two aforementioned regimes occurs when $\lambda = \tau$ and is reached by either reducing λ , through scaling down of the device dimensions (e.g., pitch), or by operating the device at cryogenic temperatures. The former is possible to implement with electron-beam (e-beam) lithography while the latter is more practical, using the fact that the τ increases with decreasing temperature [28]. In this work, we used a combination of both methods, a high frequency device (small λ) operating at cryogenic temperature (increased τ) to cross the Akhiezer regime.

2.3. Nonlinearity and Power Handling

Maximum power handling is an important criterion for filtering applications. Nonlinearity arises when input power exceeds the resonator’s power capacity. Nonlinear response compromises signal integrity and leads to the generation of intermodulation products. Operation at high frequency, unfortunately, incurs reduced energy storage capability as the resonator size is scaled down compared to larger quartz resonators [29]. Among various sources of nonlinearity in MEMS resonators, thermal nonlinearity has been identified to be the main limiter of the power handling of AlN Lamb wave resonators [30]. Thermal nonlinearity is manifested by the self-heating of the device when some of the input energy is converted to heat within the resonator body (Joule heating). Self-heating reduces the Young’s modulus of the piezoelectric film, thus lowering the resonance frequency. Downward shift in the resonance frequency, in turn, increases device impedance at a given frequency, which increases the amplitude of oscillations and results in further decrease of the resonance frequency. Non-linear response is usually captured through the amplitude versus frequency ($A-f$) response and can be described through the equation of motion of a forced Duffing oscillator:

$$m\ddot{x} + \gamma\dot{x} + kx + \alpha x^3 = F(t) \quad (6)$$

where m is the total mass, γ controls the amount of damping, k controls the linear stiffness and α controls the amount of non-linearity in the restoring force. When the oscillator trajectory depends on the initial conditions, the system can be assumed to be weakly non-linear and analysis can be restricted up to second-order non-linear terms. In such a case, at high enough power levels there is an observed bifurcation response in the

amplitude-frequency response with two possible solutions for the equilibrium temperature near resonance. As the input power is increased further, the nonlinear cubic coefficient becomes non negligible, resulting in a disturbed resonance response with the eventual appearance of hysteresis with three solutions for the equilibrium temperature. The third order nonlinearity coefficient, α , was derived for a CMR with a bottom floating electrode in [31] and expressed as:

$$\alpha = TCFR_{TH}(R_M + R_S)\omega_0^2 \quad (7)$$

To apply this formula for LFE CLMR, Equation (7) was re-evaluated. Specifically, ω_0^2 term was substituted with the linear frequency adopted from [32] for degenerate CLMR modes

$$f_r \approx \frac{1}{2T_{AlN}} \sqrt{1 + \left(\frac{2T_{AlN}}{\lambda_x}\right)^2} \sqrt{\frac{2C_{lat}}{4\rho}} \quad (8)$$

while $R_M + R_S$ expression was almost unaltered from the one in [31] with the exception of substituting the d_{31}^2 coefficient with $\sqrt{d_{33}^2 + d_{31}^2}$ as the CLMR mode was two-dimensional

$$R_M + R_S \approx \frac{1}{n} \frac{\pi \sum T_{R,i}}{8L} \frac{\rho^{1/2}_{eq}}{E^{3/2}_{eq} \sqrt{d_{31}^2 + d_{33}^2} Q} \quad (9)$$

where n denotes the number of metal electrode pairs and $T_{R,i}$, ρ_{eq} and E_{eq} are the equivalent layer stack thickness, density and Young's modulus, respectively. The thermal resistance, R_{TH} , of the narrowly anchored resonator in [31] is expressed as

$$R_{TH} = \frac{L_t}{\sum k_i T_{R,i} W_t} \quad (10)$$

where L_t , W_t and $T_{R,i}$ are the length, width and total thickness of the layers comprising anchors and $\sum k_i$ is the material stack conductivity. After substituting Equations (8)–(10) into Equation (7), the α coefficient can be expressed in terms of the geometry and material properties of AlN CLMRs. To simplify the analysis, $\sum T_{R,i}$ and $\sum \rho_{eq}$ were set to be equal to T_{AlN} and ρ , assuming the top electrode thickness was much smaller compared to the thickness of AlN. After some simplifications, α can be expressed as

$$\alpha = TCF \cdot \frac{\pi^3}{8n} \frac{L_t}{\sum k_i W_t L} \cdot \frac{1}{E^{3/2}_{eq} \sqrt{d_{31}^2 + d_{33}^2} Q} \cdot \frac{C_{lat}}{2\rho^{1/2}} \cdot \left(\frac{1}{\sum T_{R,i}^2} + \frac{2}{W_e^2} \right) \quad (11)$$

From Equation (11) it is evident that scaling the device geometry to operate at higher frequencies (small $T_{R,i}$ and W_e) results in increased nonlinearity. A larger device area (large n and L), and a wider and shorter anchor geometry, can be used to reduce the α coefficient. Higher Q , d_{31} and d_{33} coefficients can also aid in the reduction of nonlinearity. While often geometrical dimensions of the active area cannot be easily modified, anchor geometry is not critical and is more available for alterations. Hence, in this work we demonstrated the experimental results on the power handling of CLMRs with three different anchor widths.

3. Fabrication

The AlN and AlScN CLMRs were fabricated on a high resistivity wafer with an identical fabrication flow, as outlined in Figure 4.

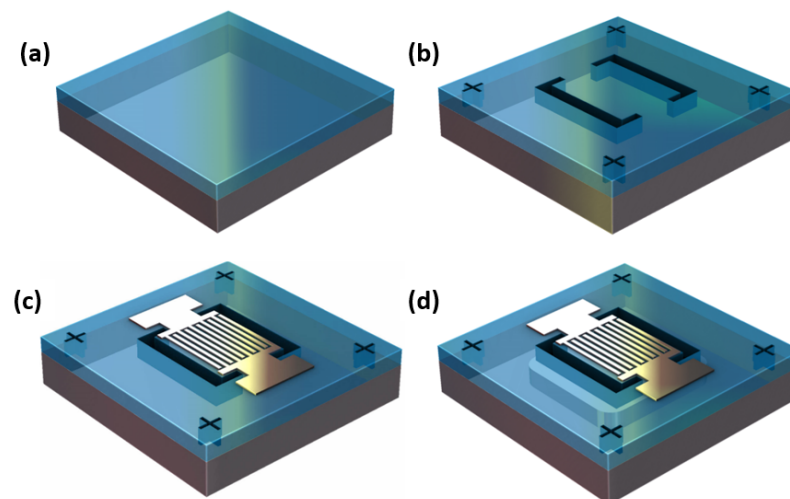


Figure 4. Fabrication steps of CLMR. (a) deposition of piezoelectric layer. (b) Reactive ion etching (RIE) of AlN/AlScN trenches and alignment marks. (c) Lift-off of 40 nm Al patterned using Electron Beam Lithography (EBL) tool. (d) dry release in XeF_2 .

An amount of 383 nm of AlN were deposited externally using the Tegal AlN Sputtering System at Carnegie Mellon University with a Full-Width-at Half-Maximum (FWHM) value of 1.5° , exhibiting excellent crystallinity. Then, 300 nm of $Al_{72}Sc_{28}N$ film was deposited using an in-house EVATEC CLUSTERLINE 200 MSQ multi-source system with Al and Sc 4-inch targets. Deposition started after a long conditioning of the chamber to reach a base pressure in the 10^{-8} mbar range and after the deposition of two dummy wafers with the same process parameters as for the production wafers. In between each run, a paste-poison procedure was used to have a consistent surface on the sputtering targets. The deposition, at $350^\circ C$, used 900 DC W + 100 RF W on the Al target and 450 W on the Sc target. The power on the Sc target was pulsed at 150 kHz with 88% duty cycle. Nitrogen, in the amount of 20 sccm and no argon were used in the sputtering, with the substrate positioned at a distance of 33 cm from the target. Crystalline quality of the resultant film was assessed via XRD measurements, as shown in Figure 5a, where a FWHM of 2.2° was extracted from the omega scan. Along with the good crystallinity, a Scanning Electron Micrograph (SEM) of the film revealed low to no occurrence of Abnormally Oriented Grains (AOGs), as shown in Figure 5b.

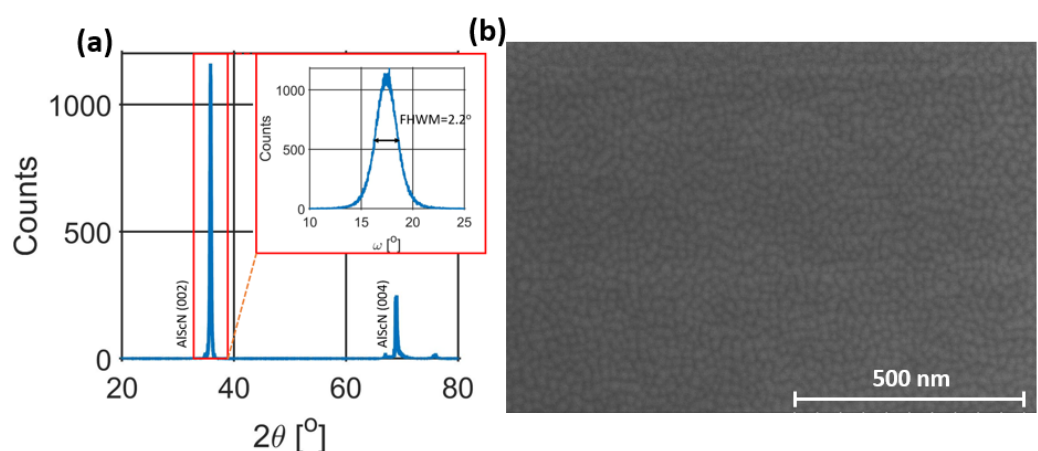


Figure 5. (a) XRD 2θ scan patterns with Rocking curves of 002 $Al_{72}Sc_{28}N$ diffraction peaks shown in the inset. (b) SEM micrograph of $Al_{72}Sc_{28}N$ film.

The piezoelectric film deposition shown in Figure 4a was followed by Plasma-enhanced Chemical Vapor Deposition (PECVD) of 700 μm of SiO_2 , used as a hard mask. The mask

was then used for the etching of $\text{Al}_{72}\text{Sc}_{28}\text{N}$ trenches and alignment marks (Figure 4b) used for the subsequent layer. The dry etch recipe of $\text{Al}_{72}\text{Sc}_{28}\text{N}$ was similar to the one described in [10], with the exception of using 400 W bias power to get a higher sidewall angle. The remaining hard mask layer was removed in Buffered Oxide Etchant (BOE). A dry etch was performed prior to Al top electrode deposition in order to avoid metal lift-off in BOE. Next, a thin layer of PMMA was spun on the surface, followed by the top electrode pattern being transferred through e-beam exposure. Exposed regions were removed in cooled solvent to improve the resist contrast. The exposure dose and the development time were tightly controlled in order to resolve the 100 nm-wide features, shown in Figure 6, that were prone to breakage due to the high aspect ratio of the fingers. E-beam lithography was followed by thermal evaporation of 40 nm of the top Al electrode and its subsequent lift-off (Figure 4c). Finally, the devices were released in XeF_2 (Figure 4d).

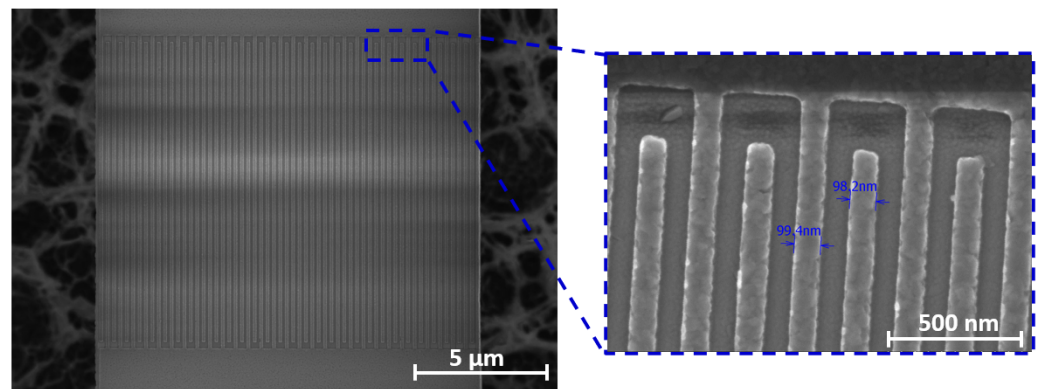


Figure 6. SEM micrograph of released 60-finger AlScN CLMR with the zoomed in view of ~100 nm wide finger electrodes shown in the inset.

4. Results and Discussion

Resonator performance was assessed by recording the S11 parameters and converting them into the admittance response. Measurements were performed using a Vector Network Analyzer (VNA, model: Keysight PNA N5221A) with -20 dBm power level and 50Ω port impedance. Resonator behavior was represented by an equivalent modified Butterworth–Van Dyke (mBVD) model [33], where motional (R_m , L_m , C_m) and static (C_0 , R_o , R_s) lumped parameters were fitted to a given resonator S11 response. Extracting the R_s value from the mBVD fitting required a long frequency span and was often not accurate. Instead, in this work, R_s values were calculated based on the electrode geometry and measured Al sheet resistance, according to Equation (5), and manually fixed in the mBVD model. Excluding R_s loading, the motional Q factor, Q_m , was estimated according to the following equation

$$Q_m = \frac{2\pi f_s L_m}{R_m} \quad (12)$$

while k_t^2 is calculated as

$$k_t^2 = \frac{\pi^2 C_m}{8 C_0} \quad (13)$$

Figure 7 compares the performances of AlN and $\text{Al}_{72}\text{Sc}_{28}\text{N}$ CLMRs with color-coded arrows pointing to the corresponding simulated k_t^2 values. To achieve similar resonant frequency AlN and $\text{Al}_{72}\text{Sc}_{28}\text{N}$ film thicknesses were set to 383 nm and 300 nm, respectively, while the corresponding pitch values were 415 nm and 300 nm. Both devices were fabricated using an identical fabrication flow. $\text{Al}_{72}\text{Sc}_{28}\text{N}$ CLMRs showed $\sim 3\times$ higher k_t^2 compared to AlN CLMRs, while their Q_m values were on par. Measured k_t^2 of $\text{Al}_{72}\text{Sc}_{28}\text{N}$ CLMR was 6.14% while for AlN CLMR it was 2%. k_t^2 values for both resonators were close to what was predicted by COMSOL ®2D, implying excellent film quality of both materials. R_s value of AlN CLMR was slightly higher, due to the smaller pitch. Overall, $\text{Al}_{72}\text{Sc}_{28}\text{N}$

CLMRs showed an enhanced response with an FoM of 15.9 compared to 4.02 for the AIN CLMR. $\sim 4\times$ improvement in the FoM of $\text{Al}_{72}\text{Sc}_{28}\text{N}$ CLMR was encouraging for the early steps of the device development.

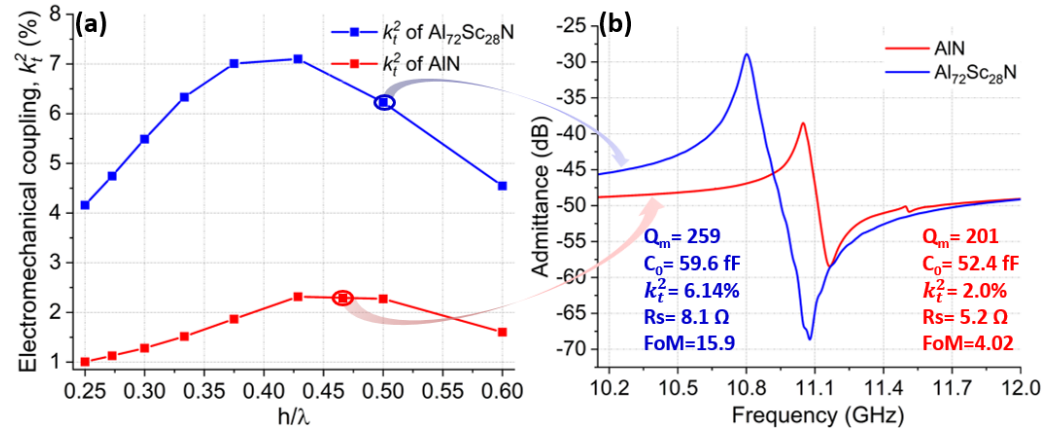


Figure 7. (a) Simulated k_t^2 of AIN (red) and AlScN (blue) over a range of h/λ_x values. (b) measured admittance response of AIN and $\text{Al}_{72}\text{Sc}_{28}\text{N}$ CLMRs operating around 11 GHz with respective arrows indicating expected k_t^2 values.

Frequency tunability of $\text{Al}_{72}\text{Sc}_{28}\text{N}$ CLMR was demonstrated in Figure 8, where magnitude (top row) and phase of the admittance responses measured from three CLMR devices with varied pitch were fitted to the MBVD model (dashed line). Figure 8a,b demonstrates the frequency tuning effect when h/λ was around the optimum value with $k_t^2 > 5\%$, while Δf was ~ 2 GHz. Figure 8c shows the potential of tuning the frequencies up to 13 GHz, which is the highest among all demonstrated piezoelectric CLMRs up to date. To note, in Figure 8c, even the k_t^2 degraded to $\sim 0.9\%$ for the CLMR with h/λ away from the optimum, as expected, but the mechanical Q remained above 300. A quick summary of the three devices is provided in Table 1.

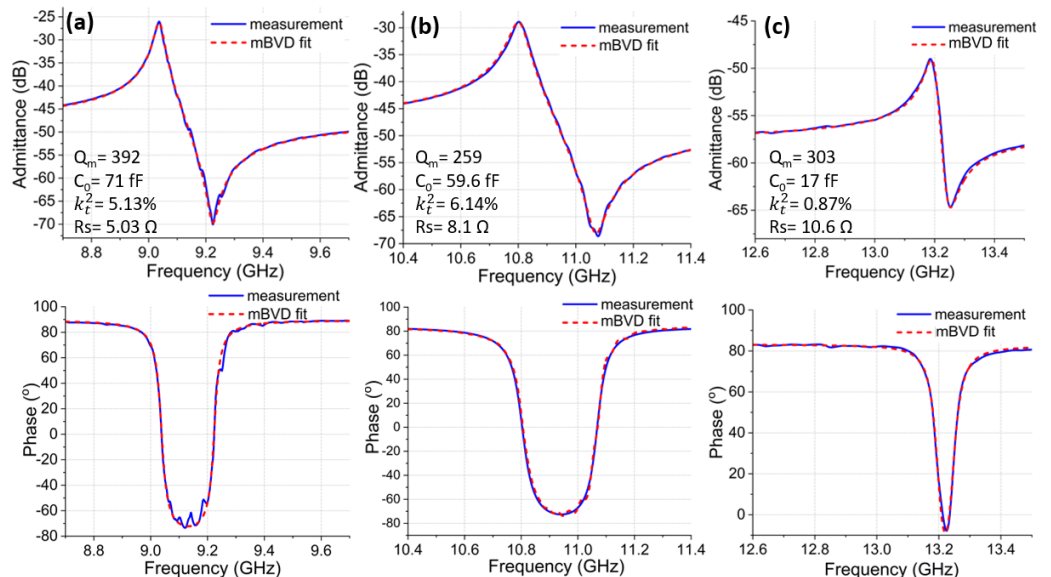
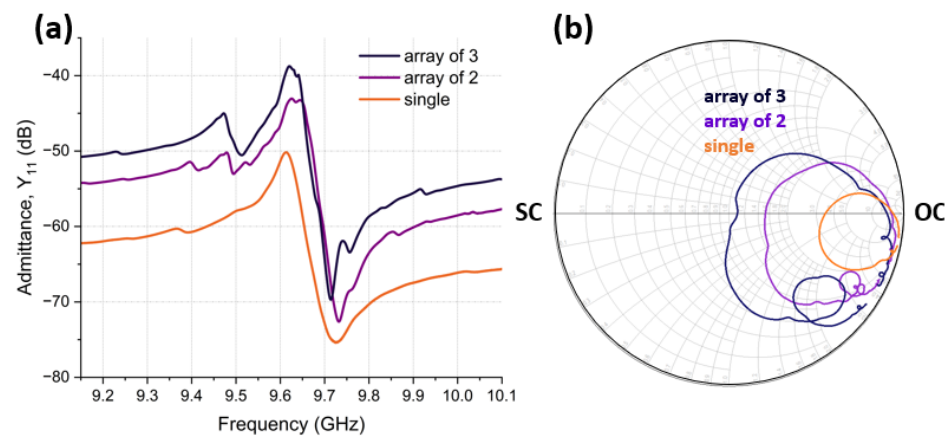


Figure 8. Admittance (top) and phase (bottom) response of $\text{Al}_{72}\text{Sc}_{28}\text{N}$ CLMRs fitted to the mBVD model: (a) CLMR operating at 9.04 GHz with $W_e = 445$ nm. (b) CLMR operating at 10.8 GHz $W_e = 300$ nm. (c) CLMR operating at 13.19 GHz $W_e = 150$ nm.

Table 1. Summary of the three CLMRs reported in Figure 8.

Device #	Pitch	Frequency	k_t^2	Q_m
1	445 nm	9.04 GHz	5.13%	392
2	300 nm	10.8 GHz	6.14%	259
3	150 nm	13.19 GHz	0.87%	303

To match to 50Ω , around which most RF systems are designed, C_0 can be tuned by forming arrays of identical CLMRs in parallel, and, thus, lowering the total impedance. Figure 9 demonstrates the admittance response of a single CLMR, an array of 2 CLMRs and an array of 3 CLMRs. As can be observed, C_0 increased as the number of array elements grew, and, thus, reached the center of the Smith Chart. Specifically, the capacitance increased from 30 fF for the single device to 90 fF for the array of 3 CLMRs, corresponding to an impedance decrease from 551Ω to 184Ω . For ease of visualization, impedance scaling was also demonstrated on the Smith Chart (Figure 9b), where, with each additional array element, circles approached the center of the Smith Chart.

**Figure 9.** Impedance scaling: (a) Admittance response of a single CLMR, array of 2 CLMRs, and array of 3 CLMRs. (b) Impedance scaling shown on the Smith Chart.

A second technique to increase C_0 involves increasing the length of the IDT fingers, L_e , keeping in mind that R_{IDT} , and, thus R_s increases, accordingly. This impacts the 3 dB Q factor, Q_{3dB} , thereby increasing electrical losses ($1/Q_{el}$). This was confirmed in Figure 10a, where, by incrementally increasing L_e Q_{3dB} decreased. Another complication associated with longer L_e is increased susceptibility to device buckling, which often results in mechanical failure of the device upon release. Stress gradients are usually the main source of bending of microbridge structures after the underlying Si is removed [34–36]. Out-of-plane bending increases in amplitude in released CLMRs with longer L_e , as shown in Figure 10. A 3D view of each device (Figure 10b) and out-of-plane bending amplitude (Figure 10c) were recorded using a Zygo optical profiler. Increased bending could possibly degrade Q factor through increased interfacial losses. However, more rigorous investigations are required to draw any conclusions.

As mentioned previously, another geometrical dimension of the CLMR that needs attention is the so-called “overhang” d . Figure 11 demonstrates simulated (a) and measured (b) admittance responses of three resonators with different d dimensions, which were otherwise identical. Most notably, when d was equal to $\lambda_x/4$ or $3\lambda_x/4$, the admittance response was relatively clean. However, when $d = \lambda_x/2$, the main mode split into two separate ones with a similar energy distribution. Figure 11c shows the shape of the two modes that appeared in $d = \lambda_x/2$ case. A lower frequency mode appearing at 9.36 GHz still resembled the main mode because its frequency was set by both the AlScN layer and the top Al electrode. The second mode appearing at 9.56 GHz, on the other hand, originated from the sustenance of the resonance set by the non-metalized portions of the plate. Specifically,

with d set to $\lambda_x/2$, cumulative non-metalized lateral distance on both ends of the plate became equal to one wavelength, thus allowing the plate edges that were free of metal to generate a higher frequency. To avoid the overlap of both frequencies that differed by the impact of metal loading, the distance d should be anything but an integer multiple of $\lambda_x/2$.

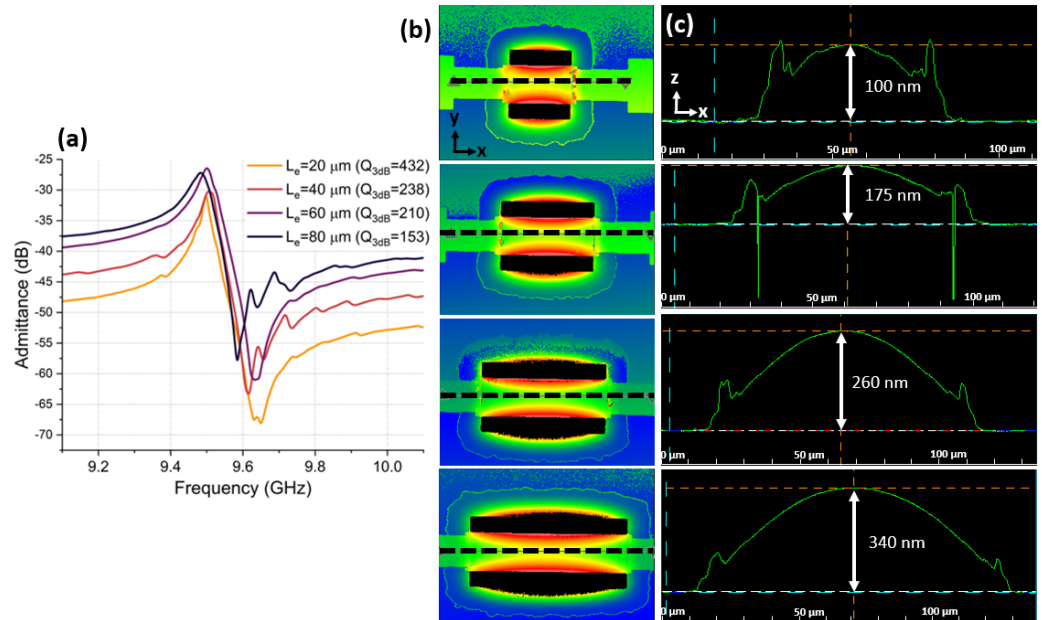


Figure 10. (a) Measured Q_{3dB} of CLMRs with different L_e . (b) 3D ZYGO measurement of top surface view of CLMRs with different L_e . (c) 2D ZYGO measurement of out-of-plane bending amplitude for each L_e .

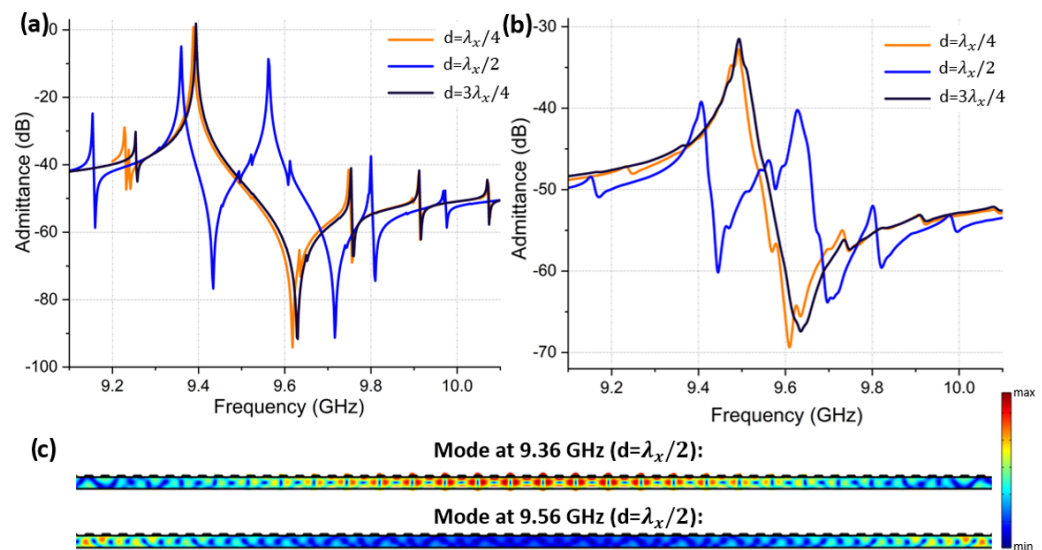


Figure 11. (a) Simulated admittance response of CLMR with d set to $\lambda_x/4$, $\lambda_x/2$ and $3\lambda_x/4$. (b) Measured admittance response of CLMR with d set to $\lambda_x/4$, $\lambda_x/2$ and $3\lambda_x/4$. (c) Mode shape of the two modes that appeared in the admittance response when $\lambda_x/2$.

To further investigate the sources of energy loss relevant to SHF CLMRs, 30 resonators identical to the device #1, from Table 1, were tested in air and vacuum (1×10^{-5} Torr), and their Q_m values compared in Figure 12. No significant difference between the two data sets was observed. This was expected, as gas (viscous) losses become negligible as operational frequencies are increased. This was confirmed by the statistical summary shown in Figure 12b, where the mean of Q_m in air vs vacuum was 271 vs. 278, respectively. This

experiment indicated that the complexity and cost of vacuum packaging can be avoided for this device topology.

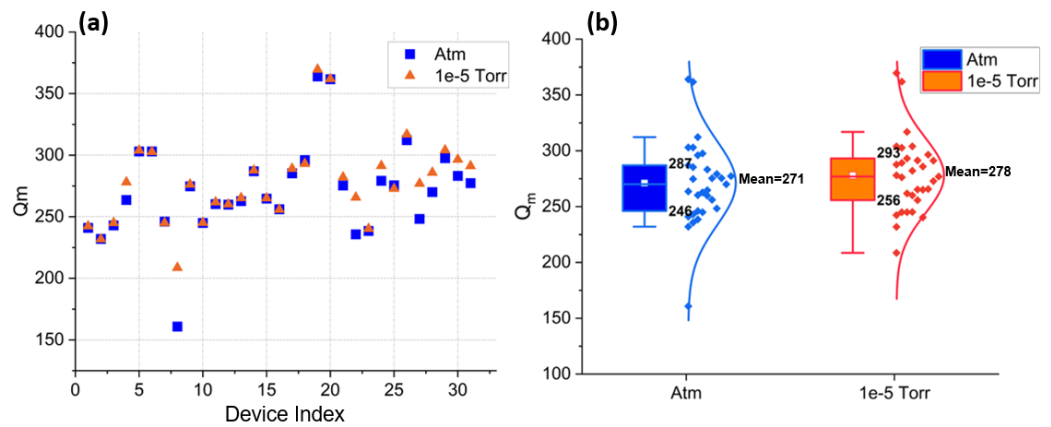


Figure 12. (a) Q_m of 30 devices measured in air (atm) vs high vacuum (1×10^{-5}). (b) The statistical summary of the Q_m in air and in a vacuum is represented as boxes with length determined by 25% and 75% percentile and corresponding normal curve distribution.

In the next experiment, Q_m of CLMRs, with three different top electrode coverage ratios (40%, 50% and 60%), was extracted and averaged over 3 identical devices, as shown in Figure 13a. Q_m did not show the trend that would prove existence of significant TED losses in metal electrodes. This was expected, since metal electrodes were placed atop minimum displacement point of the Lamé mode. To get further insight into the intrinsic material losses, two identical resonators were tested at cryogenic temperatures. Cryogenic experiments were conducted using a Lakeshore probe station with a constant chamber pressure (1×10^{-3} Torr). As demonstrated in Figure 13b, the Q_m of both devices followed a similar trend as the temperature was reduced. Most interestingly, a dip in Q_m was observed at 110 K, which coincided with the predicted Akheiser regime point for AlN [25], assuming $f \cdot Q$ over frequency plot of $Al_{72}Sc_{28}N$ would not differ significantly from that of AlN. Deriving the exact relationship of $f \cdot Q$ over frequency for various Sc doping levels is under investigation. As the temperature was further decreased, Q_m started to increase at a greater rate, signaling a transition into the Landau–Rumer regime. Overall, Q_m showed an almost $2 \times$ improvement in magnitude compared to the Q_m measured at room temperature. However, a weak dependence of Q_m on temperature until 110 K implied the existence of other loss mechanisms, which shall be a subject of future research.

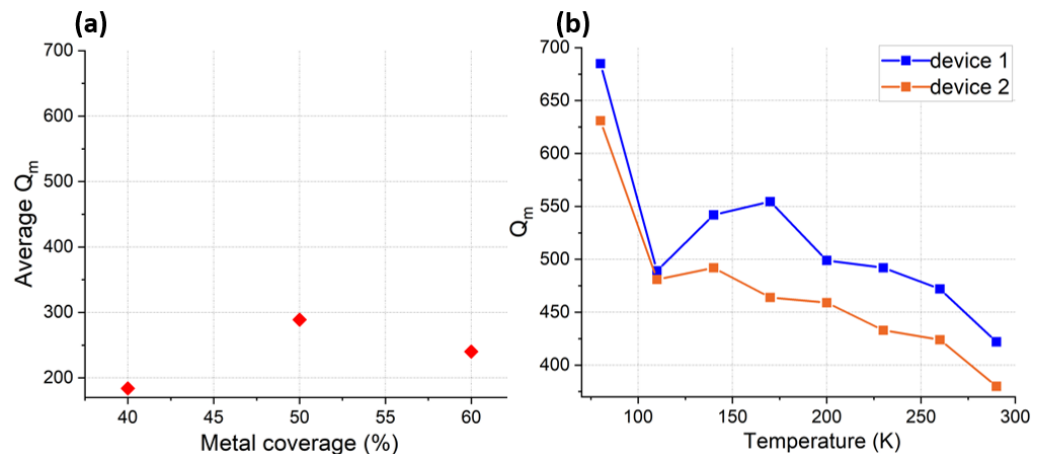


Figure 13. (a) Q_m of CLMRs with different metal coverage ratios averaged over three identical devices. (b) Q_m of two identical CLMRs measured from room temperature down to 80 K in steps of 30 K.

Next, we examined the impact of the anchor design on the mechanical anchor loss and power handling of SHF CLMRs. The three resonators that were tested are depicted in Figure 14a–c. The resonator with wide anchors, shown in Figure 14c, was identical to the device#1 from Table 1, while the other two also had similar dimensions, with the exception of the anchor widths. As mentioned previously, anchor losses are not considered to be significant at high frequencies (>1 GHz), which was confirmed by looking at the total displacement amplitude of the fully anchored CLMR simulated in COMSOL®3D, shown in Figure 14d, with a perfectly matched layer (PML) used to create absorbent boundary conditions. Given the available computer specifications, only a quarter of a 30-finger CLMR could be simulated with a finely resolved mesh (minimum element quality >0.1). As can be noticed, the displacement was localized around the center of the resonator's active area with zero displacement amplitude found at the anchors. Such a feature rendered minimum anchor loss in the mechanical domain through the anchors, which was indicated as the legends, shown in Figure 15. The Q_m -value did not show a significant variation among the three of these designs. This promises that there is a good opportunity to have large anchors for better power handling without sacrifice of the quality factor.

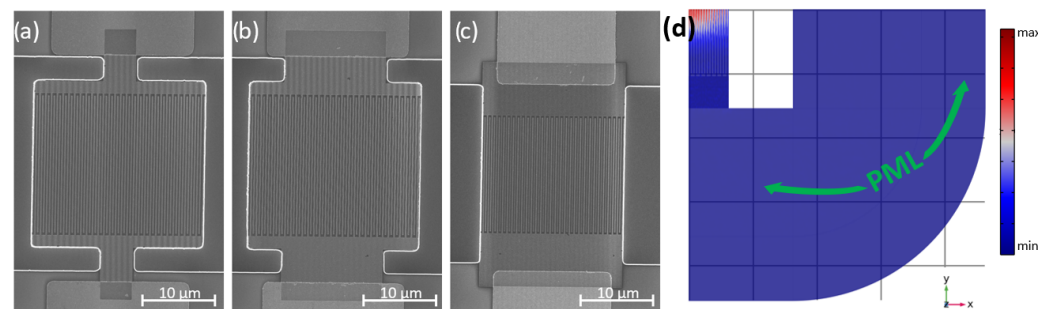


Figure 14. SEM micrographs and admittance responses of the three devices with different anchors: (a) SEM of CLMR with narrow anchor. (b) SEM of CLMR with medium anchors. (c) SEM of CLMR with wide anchors. (d) Total displacement amplitude at resonance frequency of fully anchored CLMR simulated in COMSOL®3D.

Given the above, we could continue to evaluate the nonlinearity and power handling among these three different anchor designs by examining the response of the duffing-like phenomenon at increased power levels. Figure 15 shows a zoomed-in view of the A - f response evolution as the input power, P_{in} , was swept from -10 dB to $+5$, $+7$, and $+8$ dB over 200 MHz, with 22,222 points for CLMRs with narrow, medium and wide anchors. To fulfil the steady-state condition, the IF bandwidth was set to 400 Hz to ensure the sampling time was bigger than the thermal time constant. In this way, both thermal nonlinearity and mechanical nonlinearity could be assessed [31]. The onset of the nonlinear behavior for the narrow anchor design (Figure 15a) happened when P_{in} was around 0 dBm and at $+5$ dBm a clear bifurcation in the A - f response was observed. For the medium anchor design (Figure 15b), the onset of the nonlinear behavior and the subsequent bifurcation took place when P_{in} was equal to $+5$ dBm and $+7$ dBm, respectively. Lastly, for the wide anchor design (Figure 15c) the nonlinear response became apparent between $+5$ dBm and $+7$ dBm with a clear bifurcation happening when $P_{in} = +8$ dB. As expected, among the three anchor designs, the wider anchors provided the CLMRs with better power handling, which also confirmed earlier-derived analytical expressions for the third order nonlinearity coefficient.

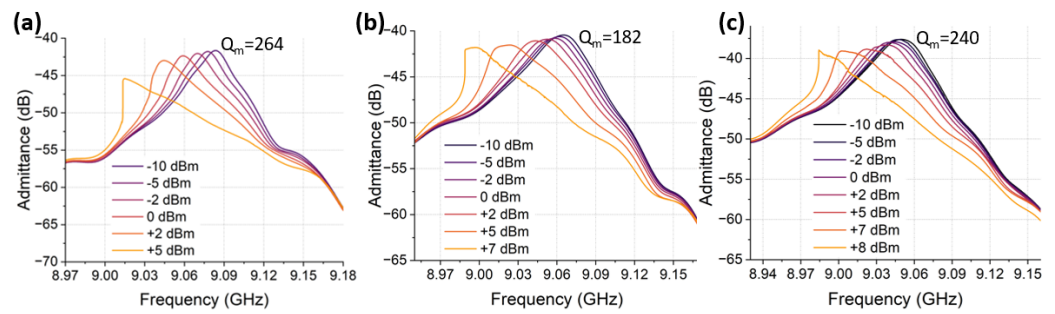


Figure 15. A- f response of SHF CLMRs at different power levels (-10 dB to $+8$ dB) : (a) A- f response of CLMR with narrow anchors. (b) A- f response of CLMR with medium anchors. (c) A- f response of CLMR with wide anchors.

Specifically, thermal nonlinearity strongly depends on the temperature coefficient of frequency (TCF), as can be seen from Equation (11). Thus, besides geometrical design, the TCF of our fabricated devices were investigated and assessed. In particular, 1st and 2nd order TCFs were compared between $\text{Al}_{72}\text{Sc}_{28}\text{N}$ and AlN CLMRs. Figure 16 depicts the admittance response recorded over a 25 – 150 °C temperature range for AlN (a) and $\text{Al}_{72}\text{Sc}_{28}\text{N}$ (b) CLMRs. TCF was calculated as the slope of Δf over ΔT and fitted to a 2nd order polynomial fit, shown in the insets, to extract linear and quadratic TCF coefficients that corresponded to the 1st and 2nd order TCF, respectively. The 1st order TCF of AlN was -28.05 ppm, which was on par with other AlN Lamb wave resonators [37]. $\text{Al}_{72}\text{Sc}_{28}\text{N}$ 1st order TCF was -35.1 ppm and was also comparable to other AlScN resonators with similar Sc doping levels [38]. $\text{Al}_{72}\text{Sc}_{28}\text{N}$ temperature stability was degraded compared to AlN , due to increased material softening with the addition of Sc. Nevertheless, thermal compensation techniques have been widely studied [39–42] and can be adopted to simultaneously improve frequency stability and power handling.

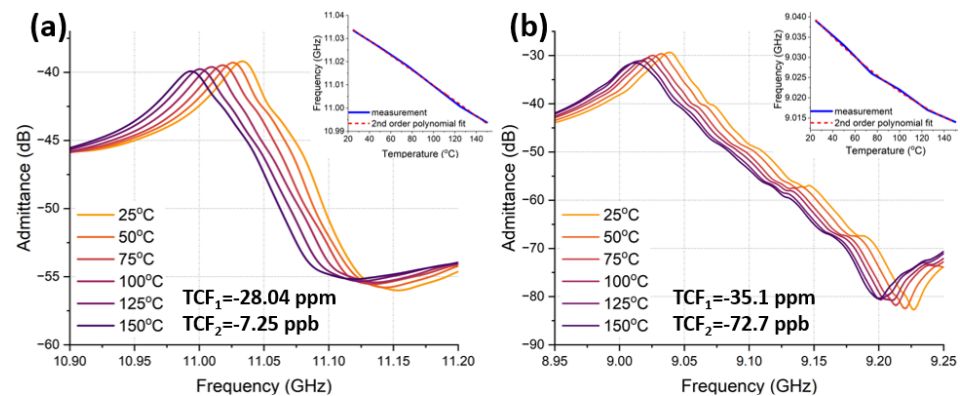


Figure 16. 1st and 2nd order TCF measured for: (a) AlN CLMR. (b) $\text{Al}_{72}\text{Sc}_{28}\text{N}$ CLMR.

Lastly, we demonstrated a monolithically integrated 2nd order ladder filter composed of $\text{Al}_{72}\text{Sc}_{28}\text{N}$ CLMRs, along with its AlN counterpart. Figure 17a shows the simulated admittance and filter responses of the constituent resonators (black straight and dashed lines) and filter (orange line) itself. The filter response was centered at the resonance frequency of the series resonator ($f_s \sim 9.15$ GHz). To maximize transmission and bandwidth, the anti-resonance frequency of the shunt CLMR was made to overlap with f_s by setting the pitch of the series and shunt resonator to be equal to 445 nm and 430 nm, respectively. Following these design parameters, we fabricated a pair of such filters with identical geometry combinations using AlN and AlScN . As demonstrated in Figure 17b, the measured S_{21} of the $\text{Al}_{72}\text{Sc}_{28}\text{N}$ filter showed a 3 dB fractional bandwidth (FBW) of $\sim 4.13\%$, which was ~ 4 times larger than the AlN implementation with a FBW of $\sim 1.18\%$. Note that the AlN filter had a higher center frequency because the resonance frequencies of the AlN CLMRs were higher than the AlScN ones for the same design, due to the variation of the materials'

elastic properties. Without any matching network, respective I.L. values of $\text{Al}_{72}\text{Sc}_{28}\text{N}$ and AIN filters were -7.7 dB and -6.12 dB, which can be improved through impedance matching as well as provisional improvement in Q . The measured out of band rejection (OBR) of the AIN filter was -13 dB and -12.7 dB as measured on both sides of the frequency spectrum, while the $\text{Al}_{72}\text{Sc}_{28}\text{N}$ filter OBR was -12.4 dB and -10.7 dB. Modest OBR was attributed to the small capacitance ratio of the shunt and series resonators (72 fF vs. 80 fF for $\text{Al}_{72}\text{Sc}_{28}\text{N}$) as well as the low filter order. Nevertheless, remarkable enhancement in the FBW of SHF CLMR filter was demonstrated by doping AIN with moderate Sc doping level (28%), signifying greater improvement should be expected at increased Sc concentrations.

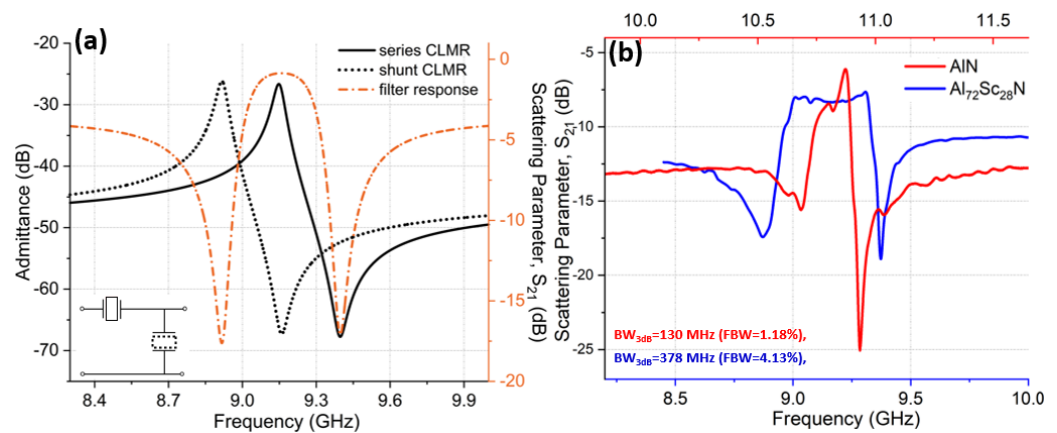


Figure 17. Simulated and measured filter response of AIN and $\text{Al}_{72}\text{Sc}_{28}\text{N}$ filters: (a) Comsol 2D simulated admittance of $\text{Al}_{72}\text{Sc}_{28}\text{N}$ series and shunt CLMRs along with the S21 scattering parameter of the 2nd order Ladder filter. (b) Measured S21 filter response of AIN and $\text{Al}_{72}\text{Sc}_{28}\text{N}$ resonators.

5. Conclusions

In this work, $\text{Al}_{72}\text{Sc}_{28}\text{N}$ CLMRs were successfully scaled to operate beyond the 6 GHz frequency range with a simple three-mask fabrication process. The FoM (~ 18) of $\text{Al}_{72}\text{Sc}_{28}\text{N}$ CLMRs surpassed that of AIN CLMRs operating around the same frequency (~ 11 GHz), by four times. In addition, a thorough analysis of loss mechanisms, power handling capacity, and frequency tuning capability were conducted to optimize our design and pave paths towards future research. Importantly, intrinsic losses were studied, and the proximity of the Akhiezer regime was identified at cryogenic temperatures. Further scaling to higher frequencies encouraged entering the Landau–Rumer regime at room temperature, where $f \cdot Q$ increased linearly with frequency. Lastly, an $\text{Al}_{72}\text{Sc}_{28}\text{N}$ 2nd order ladder filter demonstrated 4.13% FBW, which was a fourfold improvement over an identical AIN filter. The demonstrated performance enhancement achieved through the substitutional doping of Al in AIN with Sc is promising to enable advances in filtering technologies beyond 6 GHz.

Author Contributions: M.A.: Conceptualization, methodology, software, investigation, graphics, original draft preparation; M.P.: methodology; X.Z.: investigation, writing-review and editing; G.M.: methodology; P.S.: writing-review and editing; M.R.: Supervision, project administration, editing. All authors have read and agreed to the published version of the manuscript.

Funding: This work was supported by the DARPA TUFEN Program, contact number HR00112090045.

Data Availability Statement: Data are available within the article.

Acknowledgments: The authors would like to thank the staff of the George J. Kostas Nanoscale Technology and Manufacturing Research Center and Center of Nanoscale Systems at Harvard University for the assistance in device fabrication and characterization.

Conflicts of Interest: The author declares no conflict of interest.

References

1. Mahon, S. The 5G Effect on RF Filter Technologies. *IEEE Trans. Semicond. Manuf.* **2017**, *30*, 494–499. [[CrossRef](#)]
2. Felmetzger, V.V.; Laptev, P.N. Deposition of ultrathin AlN films for high frequency electroacoustic devices. *J. Vac. Sci. Technol. A* **2011**, *29*, 021014. [[CrossRef](#)]
3. Rinaldi, M.; Zuniga, C.; Piazza, G. 5–10 GHz AlN Contour-Mode Nanoelectromechanical Resonators. In Proceedings of the IEEE 22nd International Conference on Micro Electro Mechanical Systems, Sorrento, Italy, 25–29 January 2009.
4. Schaffer, Z.; Simeoni, P. 33 GHz Overmoded Bulk Acoustic Resonator. *IEEE Microw. Wirel. Components Lett.* **2022**, *32*, 656–659. [[CrossRef](#)]
5. Assylbekova, M.; Chen, G.; Michetti, G.; Pirro, M.; Colombo, L.; Rinaldi, M. 11 GHz Lateral-Field-Excited Aluminum Nitride Cross-Sectional Lamé Mode Resonator. In Proceedings of the Joint Conference of the IEEE International Frequency Control Symposium and International Symposium on Applications of Ferroelectrics (IFCS-ISAF), Keystone, CO, USA, 19–23 July 2020.
6. Cassella, C.; Hui, Y.; Qian, Z.; Hummel, G.; Rinaldi, M. Aluminum Nitride Cross-Sectional Lamé Mode Resonators. *JMEMS* **2016**, *25*, 275–285.
7. Aigner, R.; Fattinger, G.; Schaefer, M.; Karnati, K.; Rothemund, R.; Dumont, F. BAW Filters for 5G Bands. In Proceedings of the IEEE International Electron Devices Meeting (IEDM), San Francisco, CA, USA, 1–5 December 2018.
8. Akiyama, M.; Kamohara, T.; Kano, K.; Teshigahara, A.; Takeuchi, Y.; Kawahara, N. Enhancement of Piezoelectric Response in Scandium Aluminum Nitride Alloy Thin Films Prepared by Dual Reactive Cosputtering. *Adv. Mater.* **2009**, *21*, 593–596. [[CrossRef](#)] [[PubMed](#)]
9. Moe, C.; Olsson, R.H.; Patel, P.; Tang, Z.; D’Agati, M.; Winters, M.; Vetury, R.; Shealy, J. Highly Doped AlScN 3.5 GHz XBAW Resonators with 16% k_{eff} for 5G RF Filter Applications. In Proceedings of the 2020 IEEE International Ultrasonics Symposium (IUS), Las Vegas, NV, USA, 7–11 September 2020.
10. Zhao, X.; Kaya, O.; Pirro, M.; Assylbekova, M.; Colombo, L.; Simeoni, P.; Cassella, C. A 5.3 GHz Al_{0.76}Sc_{0.24}N Two-Dimensional Resonant Rods Resonator With a k_{t2} of 23.9%. *J. Microelectromech. Syst.* **2022**, *31*, 561–570. [[CrossRef](#)]
11. Park, M.; Wang, J.; Dargis, R.; Clark, A.; Ansari, A. Super High-Frequency Scandium Aluminum Nitride Crystalline Film Bulk Acoustic Resonators. In Proceedings of the IEEE International Ultrasonic Symposium (IUS), Glasgow, UK, 6–9 October 2019.
12. Park, M.; Hao, Z.; Kim, D.G.; Clark, A.; Dargis, R.; Ansari, A. A 10 GHz Single-Crystalline Scandium-Doped Aluminum Nitride Lamb-Wave Resonator. In Proceedings of the IEEE 20th International Conference on Solid-State Sensors, Actuators and Microsystems & Eurosensors XXXIII (TRANSDUCERS & EUROSENSORS XXXIII), Berlin, Germany, 23–27 June 2019.
13. Akiyama, M.; Nagao, K.; Ueno, N.; Tateyama, H.; Yamada, T. Influence of metal electrodes on crystal orientation of aluminum nitride thin films. *Vacuum* **2004**, *74*, 699–703. [[CrossRef](#)]
14. Olsson, R.H.; Wojciechowski, K.E.; Branch, D.W. Origins and mitigation of spurious modes in aluminum nitride microresonators. In Proceedings of the 2010 IEEE International Ultrasonics Symposium, San Diego, CA, USA, 11–14 October 2010.
15. Green, E.I. The Story of Q. *Am. Sci.* **1955**, *43*, 584–594.
16. Zuo, C.; Sinha, N.; Pisani, M.B.; Perez, C.R.; Mahameed, R.; Piazza, G. 12E-3 channel-select RF MEMS filters based on selfcoupled AlN contour-mode piezoelectric resonators. In Proceedings of the IEEE International Ultrasonic Symposium, New York, NY, USA, 28–31 October 2007.
17. Leeson, D.B. A simple model of feedback oscillator noise spectrum. *Proc. IEEE* **1966**, *54*, 329–330. [[CrossRef](#)]
18. Kamon, M. Computational Modeling Challenges. In *Piezoelectric MEMS Resonators*; Bhugra, H., Piazza, G., Eds.; Springer: Cham, Switzerland, 2017; pp. 257–279.
19. Cho, Y.; Pisano, A.P.; Howe, R.T. Viscous damping model for laterally oscillating microstructures. *J. Microelectromech. Syst.* **1994**, *3*, 81–87. [[CrossRef](#)]
20. Ho, G.K.; Abdolv, R.; Sivapurapu, A.; Humad, S.; Ayazi, F. Piezoelectric-on-Silicon Lateral Bulk Acoustic Wave Micromechanical Resonators. *JMEMS* **2008**, *17*, 512–520. [[CrossRef](#)]
21. Segovia-Fernandez, J.; Cremonesi, M.; Cassella, C.; Frangi, A.; Piazza, G. Anchor losses in AlN contour mode resonators. *J. Microelectromech. Syst.* **2015**, *24*, 265–275. [[CrossRef](#)]
22. Abdolv, R.; Bahreyni, B.; Lee, J.E.-Y.; Nabki, F. Micromachined Resonators: A Review. *Micromachines* **2016**, *7*, 160. [[CrossRef](#)]
23. Wauk, M.T., II; Attenuation in Microwave Acoustic Transducers and Resonators. Ph.D. Dissertation, Stanford University, Stanford, CA, USA, 1969.
24. Segovia-Fernandez, J.; Piazza, G. Thermoelastic damping in the electrodes determines Q of AlN contour mode resonators. *J. Microelectromech. Syst.* **2017**, *26*, 550–558. [[CrossRef](#)]
25. Tabrizian, R.; Rais-Zadeh, M.; Ayazi, F. Effect of phonon interactions on limiting the f_0Q product of micromechanical resonators. In Proceedings of the International Solid-State Sensors, Actuators and Microsystems Conference, Denver, CO, USA, 21–25 June 2009.
26. Ch, orkar, S.A.; Agarwal, M.; Melamud, R.C.; Ler, R.N.; Goodson, K.E.; Kenny, T.W. Limits of quality factor in bulk-mode micromechanical resonators. In Proceedings of the IEEE 21st International Conference on Micro Electro Mechanical Systems, Tucson, AZ, USA, 13–17 January 2008.
27. L.; au, L.; Rumer, G. Absorption of sound in solids. *Phys. Z. Sowjetunion* **1937**, *11*, 18.
28. Fon, W.; Schwab, K.C.; Worlock, J.M.; Roukes, M.L. Phonon scattering mechanisms in suspended nanostructures from 4 to 40 K. *Phys. Rev. B* **2002**, *66*, 045302. [[CrossRef](#)]

29. Kaajakari, V.; Mattila, T.; Oja, A.; Seppa, H. Nonlinear Limits for Single-Crystal Silicon Resonators. *JMEMS* **2004**, *13*, 715–724.
30. Tazzoli, A.; Rinaldi, M.; Plazz, G. Experimental Investigation of Thermally Induced Nonlinearities in Aluminum Nitride Contour-Mode MEMS Resonators. *IEEE Electron Device Lett.* **2012**, *33*, 724–726. [[CrossRef](#)]
31. Segovia-Fernandez, J.; Piazza, G. Thermal Nonlinearities in Contour Mode AlN Resonators. *J. Microelectromech. Syst.* **2013**, *22*, 976–985. [[CrossRef](#)]
32. Cassella, C.; Qian, Z.; Hummel, G.; Rinaldi, M. 1.02 GHz cross-sectional Lamé mode resonator with high KT2 exceeding 4.6%. In Proceedings of the 2016 IEEE 29th International Conference on Micro Electro Mechanical Systems (MEMS), Shanghai, China, 24–28 January 2016.
33. Lu, R.; Li, M.; Yang, Y.; Manzanque, T.; Gong, S. Accurate extraction of electromechanical coupling in piezoelectric MEMS resonators. *J. Microelectromech. Syst.* **2019**, *28*, 209–218. [[CrossRef](#)]
34. Fang, W.; Lee, C.-H.; Hu, H.-H. On the buckling behavior of micromachined beams. *J. Micromech. Microeng.* **1999**, *9*, 236–244. [[CrossRef](#)]
35. Fang, W.; Wickert, J.A. Determining mean and gradient residual stresses in thin films using micromachined cantilevers. *J. Micromech. Microeng.* **1996**, *6*, 301–309. [[CrossRef](#)]
36. Chu, W.-H.; Mehregany, M. A study of residual stress distribution through the thickness of p+ silicon film. *J. IEEE Trans. Electron Dev.* **1993**, *40*, 1245–1250. [[CrossRef](#)]
37. Fei, S.; Ren, H. Temperature Characteristics of Contour Mode MEMS AlN Piezoelectric Ring Resonator on SOI Substrate. *Micromachines* **2021**, *12*, 143. [[CrossRef](#)] [[PubMed](#)]
38. Hashimoto, K.; Fujii, T.; Sato, S.; Omori, T.; Ahn, C.; Teshigahara, A.; Kano, K.; Umezawa, H.; Shikata, S. High Q Surface Acoustic Wave Resonators in 2-3 GHz Range Using ScAlN/Single Crystalline Diamond Structure. In Proceedings of the International Ultrasonic Symposium, Dresden, Germany, 7–10 October 2012.
39. Lin, C.; Yen, T.; Lai, Y.; Felmetsger, V.V.; Hopcroft, M.A.; Kuypers, J.H.; Pisano, A.P. Temperature-compensated aluminum nitride lamb wave resonators. *IEEE Int. Ultrason. Ferroelectr. Freq. Control* **2010**, *57*, 524–532. [[CrossRef](#)] [[PubMed](#)]
40. Wingqvist, G.; Arapan, L.; Yantchev, V.; Katardjiev, I. Temperature compensation of thin AlN film resonators utilizing the lowest order symmetric lamb mode. In Proceedings of the IEEE Ultrasonic Symposium, Beijing, China, 2–5 November 2008.
41. Kuypers, J.H.; Lin, C.; Vigevani, G.; Pisano, A.P. Intrinsic temperature compensation of aluminum nitride Lamb wave resonators for multiple-frequency references. In Proceedings of the IEEE International Frequency Control Symposium, Honolulu, HI, USA, 19–21 May 2008.
42. Zhao, X.; Kaya, O.; Pirro, M.; Kang, S.; Cassella, C. Improving Thermal Linearity and Quality Factor of Al72Sc28N Contour Mode Resonators Using Acoustic Metamaterials based Lateral Anchors. In Proceedings of the IEEE 2022 Joint Conference of the European Frequency and Time Forum and IEEE International Frequency Control Symposium (EFTF/IFCS), Paris, France, 24–28 April 2022.

Disclaimer/Publisher’s Note: The statements, opinions and data contained in all publications are solely those of the individual author(s) and contributor(s) and not of MDPI and/or the editor(s). MDPI and/or the editor(s) disclaim responsibility for any injury to people or property resulting from any ideas, methods, instructions or products referred to in the content.